Article

Controllable dimensionality conversion between 1D and 2D CrCl$_3$ magnetic nanostructures

Shuangzan Lu [1,2,7], Deping Guo [3,4,7], Zhengbo Cheng[1,7], Yanping Guo[1,7], Cong Wang [3,4], Jinghao Deng [1], Yusong Bai[1], Cheng Tian [5], Linwei Zhou [3,4], Youguo Shi[5], Jun He [1,6] ✉, Wei Ji [3,4] ✉ & Chendong Zhang [1] ✉

The fabrication of one-dimensional (1D) magnetic systems on solid surfaces, although of high fundamental interest, has yet to be achieved for a crossover between two-dimensional (2D) magnetic layers and their associated 1D spin chain systems. In this study, we report the fabrication of 1D single-unit-cell-width CrCl$_3$ atomic wires and their stacked few-wire arrays on the surface of a van der Waals (vdW) superconductor NbSe$_2$. Scanning tunneling microscopy/spectroscopy and first-principles calculations jointly revealed that the single wire shows an antiferromagnetic large-bandgap semiconducting state in an unexplored structure different from the well-known 2D CrCl$_3$ phase. Competition among the total energies and nanostructure-substrate interfacial interactions of these two phases result in the appearance of the 1D phase. This phase was transformable to the 2D phase either prior to or after the growth for in situ or ex situ manipulations, in which the electronic interactions at the vdW interface play a nontrivial role that could regulate the dimensionality conversion and structural transformation between the 1D-2D CrCl$_3$ phases.

Tailoring two-dimensional (2D) materials into one-dimensional (1D) structures, such as nanoribbons and nanowires, has been a prevailing approach for the manufacture of emergent properties in van der Waals (vdW) structures. Extensive attempts have been made to achieve controlled fabrication of the 1D counterparts of graphene[1–3] and semiconducting transition metal chalcogenides[4–6], which have exhibited rich electron-correlated behaviors[5,6]. The recent discovery of long-range magnetism in atomically thin vdW materials, e.g., chromium trihalides, is a major breakthrough in the field of 2D materials. This discovery has opened up a new avenue for the applications of vdW structures in spintronics[7–14]. The integration of 1D and 2D magnetic nanostructures appears to be a promising strategy for minimizing the size of spintronic devices[15,16]. The direct growth of 1D nanostructures on 2D layers is a straightforward strategy for 1D–2D vdW integration, which naturally raises the question of whether the 1D counterparts of these emerging 2D magnetic materials can be obtained on 2D substrates.

One-dimensional magnetic systems, usually in the form of spin chains, are themselves a thriving field of research and have been used to illustrate many key concepts in many-body quantum physics[17] and even triggered the recent search for new phases of matter (such as the Majorana fermion)[18–21]. Note that in a practical prototypic system, spin-chain excitations strongly depend on the coupling with the environment, mostly the holding substrate. Various ways exist to create

[1]School of Physics and Technology, Wuhan University, Wuhan 430072, China. [2]Hubei Jiufengshan Laboratory, Wuhan 430074, China. [3]Department of Physics and Beijing Key Laboratory of Optoelectronic Functional Materials and Micro-Nano Devices, Renmin University of China, Beijing 100872, China. [4]Key Laboratory of Quantum State Construction and Manipulation (Ministry of Education), Renmin University of China, Beijing 100872, China. [5]Beijing National Laboratory for Condensed Matter Physics and Institute of Physics, Chinese Academy of Sciences, Beijing 100190, China. [6]Wuhan Institute of Quantum Technology, Wuhan 430206, China. [7]These authors contributed equally: Shuangzan Lu, Deping Guo, Zhengbo Cheng, Yanping Guo. ✉e-mail: He-jun@whu.edu.cn; wji@ruc.edu.cn; cdzhang@whu.edu.cn

physical realizations of spin chains on solid surfaces, based on either compound solids, molecular self-assembly, or trapped atoms[21–25]. However, a spin chain with a vdW nature, which offers considerable magnetic exchange interactions within the chain and minimizes undesired interactions with the supporting substrate, has yet to be realized.

Here, our scanning tunneling microscopy/spectroscopy (STM/S) measurements and density functional theory (DFT) calculations jointly showed an exceptional category of 1D $CrCl_3$ atomic wires in a previously unobserved form. It was grown solely on an isotropic $NbSe_2$ vdW surface and was different from the nanoribbons of the 2D $CrCl_3$ phase that were also prepared in this work. Such a 1D wire, consisting of a single row of *face-sharing* $CrCl_6$ octahedra, is a large-gap semiconductor exhibiting a Néel-type antiferromagnetic (AFM) coupling. The narrowest 1D wire had a single unit-cell-width (denoted as a single-wire, SW) and could be stacked in parallel, forming vdW wire arrays. Interestingly, we observed that the STM tip triggered 1D–2D dimensional conversion, accompanied by a polymorphic phase transformation, in quad- or wider wires arrays. Our theory, along with experimental inputs, aided the understanding of the reason for the presence of the 1D phase and the subsequent 1D–2D conversion. The ability of the substrate to stabilize 1D-wire ends or 2D-flake edges by donating electrons through vdW couplings was of critical importance in controlling the dimensionality conversion and the phase transformation. Our findings refreshed the understanding of vdW epitaxy and established an alternative idea for the vdW interface engineering of 1D nanostructures.

Results

Figure 1a shows a typical STM image of $CrCl_3$ grown on a bulk $NbSe_2$ substrate with -0.15 ML coverage (see the Methods Section for experimental details). The figure clearly indicates an anisotropic growth mode in which subnanometer-width or few-nanometer-width 1D structures developed along the armchair directions of the $NbSe_2$ lattice and were jointed at small 2D flakes. This 1D–2D coexisting feature appeared to be unique on the $NbSe_2$ substrate in that an attempt at the growth of $CrCl_3$ on a bilayer graphene (BLG) surface solely led to hexagonal-like flakes (Fig. 1e). These flakes showed the lattice of the well-known 2D $CrCl_3$ monolayer (Fig. 1f), namely, periodically spaced trimers of top-layer Cl atoms (marked by the dashed triangles)[12] with a separation of 6.0 Å, which denoted the 2D phase.

In terms of the 1D–2D complexes formed on the $NbSe_2$ substrate, the small flakes were also in the 2D phase (Supplementary Fig. S1), but the 1D wires seemed to be in a different phase. A close-up look at the wires (Fig. 1b) explicitly illustrates their composition of parallelly stacked integer numbers of single atomic wires. A further zoomed-in constant-current image of a single wire is shown in Fig. 1c. The figure exhibits a zig–zag chain of protrusions with an apparent height of -6.2 Å (Supplementary Fig. S2a, b), a periodicity (c) of 6.0 Å, and a separation of 1.8 Å (labeled as d in Fig. 1c) between two rows of the zig–zag chain. All these remarkable features of the observed 1D phase differentiated it from simply an ultranarrow ribbon of the 2D $CrCl_3$ monolayer, which was, again, confirmed by the higher topographic heights of the wires than those of the 2D flakes at certain sample bias (Supplementary Fig. S2c, d).
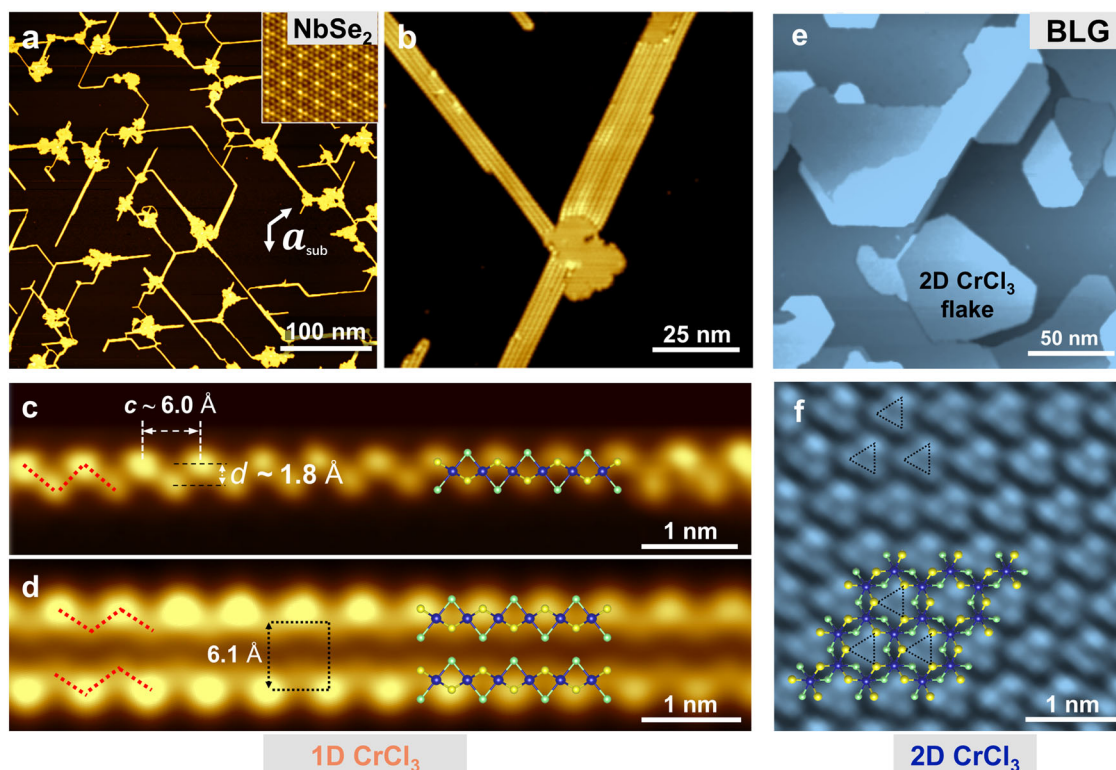

Fig. 1 | STM images of 1D CrCl3 wires on NbSe2 and 2D CrCl3 flakes on BLG. **a** STM image of $CrCl_3$ grown on a bulk $NbSe_2$ surface (1.1 V, 10 pA). The inset shows the atomically resolved STM image taken on the nearby $NbSe_2$. The prime vector a_{sub} of the $NbSe_2$ lattice is marked as shown. **b** Close-up image (1.1 V, 10 pA) showing that the as-grown 1D structures consisted of integer numbers of atomic wires, which were jointed at the small flakes. **c, d** Atomically resolved images (0.5 V, 100 pA) of the isolated $CrCl_3$ single wire and bi-wires. The schematics of the atomic models are superposed on the images. Only the topmost Cl atoms (yellow in the model) were imaged, with the formation of the zig–zag chains marked by the red dashed lines. The rectangular unit cell of the bi-wires is marked by black dashed lines. **e** Typical image (1.6 V, 5 pA) of the sample grown on BLG showing only 2D flakes with a monolayer thickness. **f** Atomically resolved image of the 2D $CrCl_3$ phase in **e** with an overlaid schematic model. The dashed black triangles indicate the Cl trimers. The small 2D flakes in **a** show the same 2D phase (Supplementary Fig. S1).
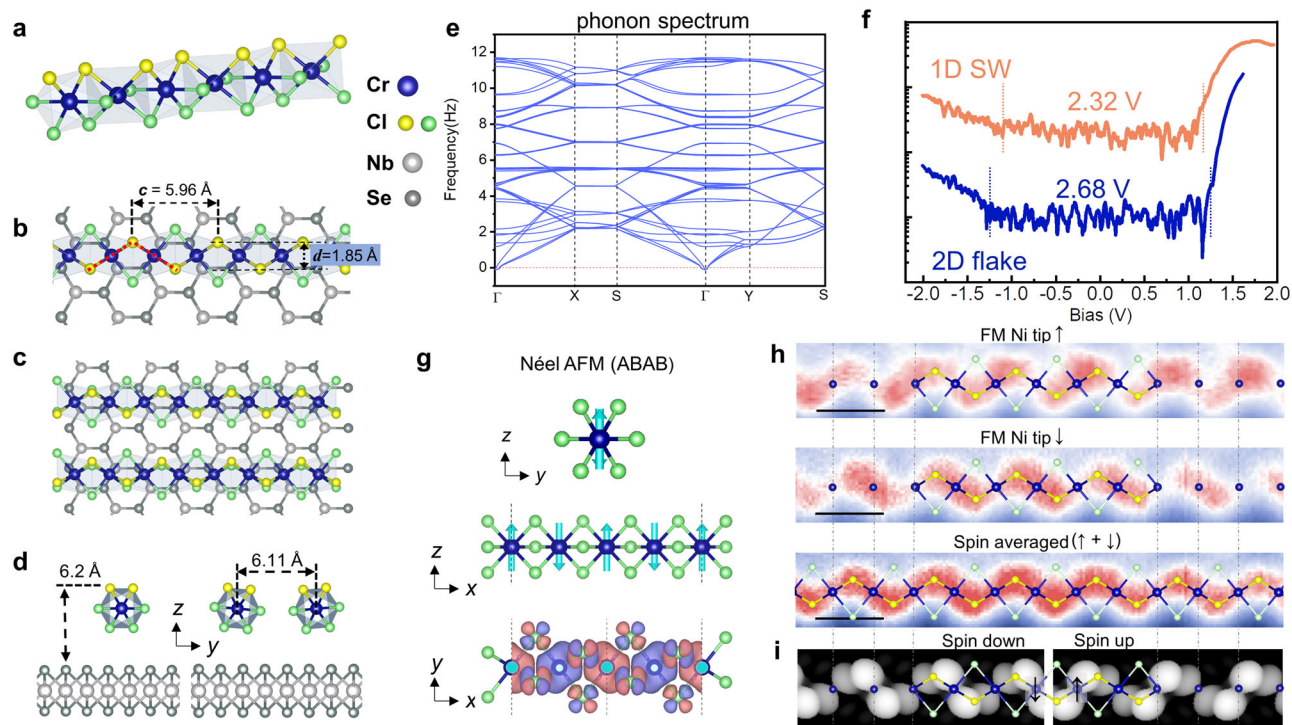
Fig. 2 | Atomic, electronic, and magnetic structures of 1D CrCl₃ wires.
a Perspective view of a single CrCl₃ wire composed of face-sharing CrCl₆ octahedra (shadowed). **b, c** Top views of the most stable configurations of the single wire and bi-wires on the adsorbed NbSe₂ obtained in our DFT calculations. The corresponding cross-sectional views are shown in (**d**). The Cr atoms are displayed in blue, and the Cl atoms are displayed in yellow (for the topmost ones) and green. **e** Calculated phonon spectrum of the CrCl₃ wire array with an infinite width. **f** Typical dI/dV spectra (on a logarithmic scale) of a single wire (orange) and a 2D CrCl₃ flake (blue). The band gap values are labeled. **g** Schematics of the spin configuration in a single wire. A total energy comparison among various magnetic

configurations indicates that the most stable configuration is the Néel AFM (ABAB) state (Supplementary Fig. S4). The arrows represent the spin directions. The lower panel shows the visual spin density distribution (red: spin-up; blue: spin-down). **h** Constant current images were taken with a spin-polarized Ni tip. The upper and middle panels show the same area imaged by the tip magnetized with +0.7 T and −0.7 T magnetic fields, respectively. Both images were acquired at +1.5 V and 5 pA. Cross-check of the contrast reversal is seen in Supplementary Fig. S5. The lower panel is a sum of the above two panels. Scale bars are 0.5 nm. The vertical grid lines represent the Cr sites (blue dots), and atomic models are superimposed on each panel. **i** Simulations of STM images with pure spin-up/downsample DOS at +1.0 V.

Thus, this unknown 1D CrCl₃ structure was referred to as the 1D phase. Its STM topographic features were analogous to those of the formerly predicted 1D polymorphic phase of CrBr₃[26]. We thus proposed that the 1D phase structure (Fig. 2a) consisted of a single Cr³⁺ row encapsulated by *face-sharing* CrCl₆ octahedra along the wire axis, showing a tube-like structure with six Cl lobes in the cross-sectional view (Fig. 2d). The 2D phase also contained the same individual octahedral units, but these units were connected to each other in an *edge-sharing* manner, as seen in the schematic model superposed in Fig. 1f. Therefore, the two phases have very different structural parameters, e.g., the Cr-Cr spacing (2.95 vs. 3.44 Å), the Cr–Cr–Cr angle (180° vs. 120°), and the Cr–Cl–Cr bond angle (77° vs. 94°). Thus, discrepancies would likely exist in the exchange interactions and the magnetic ground states between these two structures.

The DFT calculated phonon spectra of the free-standing 1D CrCl₃ wire array (Fig. 2e), and the CrCl₃ single wire (Supplementary Fig. S3a) show no imaginary frequency, manifesting the structural stability. Upon the adsorption on the NbSe₂ surface, the wire prefers to sit on the surface through two Cl lobes at the site shown in Fig. 2b, leading to another two Cl atomic rows being directed toward the vacuum (Fig. 2d). These two Cl atoms made dominant contributions to the STM imaging, and the image, therefore, yielded a zig–zag appearance like that shown in Fig. 1c. In addition, our calculations revealed the lattice constant $c = 5.96$ Å, the Cl–Cl separation $d = 1.85$ Å, and the apparent height of 6.20 Å, which were very consistent with the experimental values of 6.0, 1.8, and 6.2 Å. This good consistency was maintained in the wider wire arrays, e.g., bi-wires (Figs. 1d and 2c, d). When two wires were stacked together, the experimental image (Fig. 1d) showed a

different morphology from that of the single wire presented above in that two rows of atoms in each zig–zag chain appeared to have an apparent difference in height. This was consistent with the small tilt angle predicted by our calculations, as illustrated in the cross-sectional view (Fig. 2d, details in Supplementary Fig. S2e, f). In addition, for the interwire atomic registry, it was clearly seen in both the experimental and theoretical results that there was no shift along the wire axis between the two nearby zig–zag chains, and a rectangular unit-cell with an interwire separation of ~6.1 Å was thus formed.

Figure 2f shows typical differential conductivity (dI/dV) spectra taken for 1D SW/NbSe₂ and 2D flake/NbSe₂. The SW had an experimental bandgap of 2.32 eV, smaller than that of the 2D flake (2.68 eV). Our DFT calculations revealed that the SW prefers a Néel AFM state (Supplementary Figs. S3b and S4), showing a magnetic moment of ~2.8 μ_B primarily on each Cr atom and a bandgap of 1.25 eV (six-Cr finite wire) – 2.81 eV (infinite wire) depending on the wire length. Details of the band gap calculations are seen in Supplementary Table S1. The larger bandgap in the 2D monolayer was reproduced by our calculation in that the infinite form of the 2D phase gave a bandgap of 3.08 eV, and the six-Cr 2D-phase flake gave a bandgap of 1.52 eV. The systematically smaller experimental values could be ascribed to the finite sizes of the 1D and 2D CrCl₃ structures measured in our experiments. The easy axis of the magnetic moments was perpendicular to the wire axis direction with a magnetic anisotropic energy of 0.02 meV/Cr, as extensively discussed in Supplementary Fig. S6.

The ABAB AFM order was examined by spin-polarized STM (SP-STM) measurements[27,28]. With out-of-plane magnetic fields, the bulk Ni tip was in-situ magnetized to a spin-up (spin-down) state before
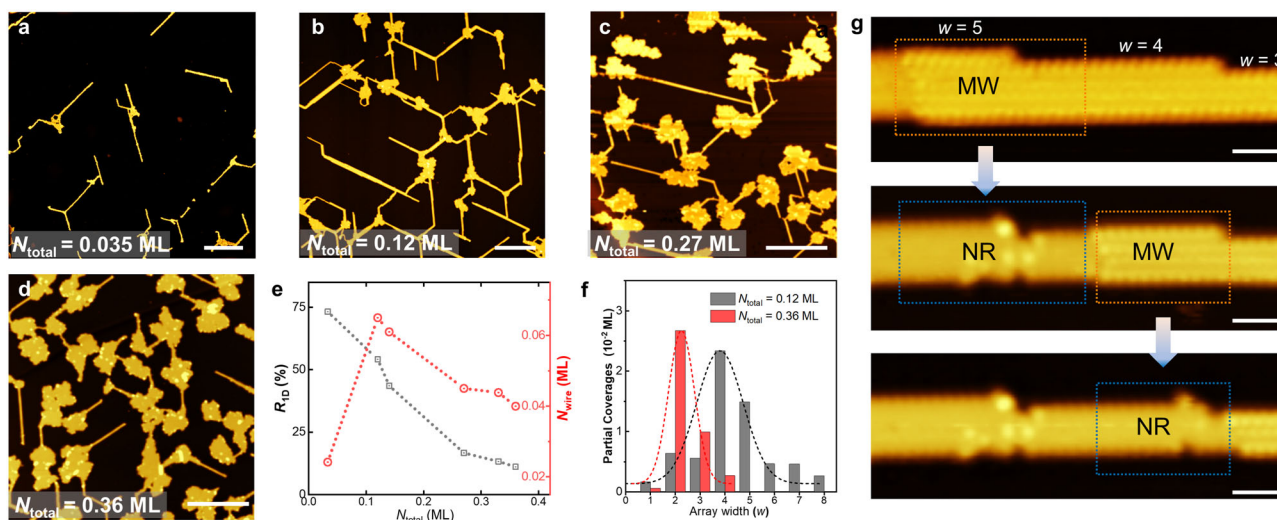
Fig. 3 | Coverage-dependent and tip-manipulated 1D-to-2D transformations. **a–d** Coverage-dependent topographic images of $CrCl_3$ grown on $NbSe_2$ with the total coverage ranging from 0.035 to 0.36 ML. Scale bars are 50 nm. **e** Plot of the coverage N_{wire} of the 1D wires and the coverage ratio $R_{1D} = N_{wire}/N_{total}$ as functions of N_{total}. **f** Statistical analysis of the widths of the wire arrays at $N_{total} = 0.12$ ML and 0.36 ML. **g** Tip-manipulated transformations from the 1D multi-wire arrays (MWs) to 2D nanoribbons (NRs). The technical details are discussed in the "Methods" section. Images were taken at −0.6 V and 10 pA; scale bars are 2 nm.

scanning [Methods]. The observations shown below were reproducible in our experiments using different Ni tips. Figure 2h shows the constant current images of the same area taken with the spin-up (upper panel) and spin-down (middle panel) tip states. The bias here was chosen to be near the conduction band edge, which hosts the maximum polarization in the density of states (DOS) (Fig. S7). It is apparent in both images that a contrast appears between adjacent Cr sites. In addition, we observed that such contrast is reversed under the flipping of the tip magnetization (up/down). For comparison, we show a spin-averaged image (lower panel in Fig. 2h) derived by adding the intensities of the two spin-resolved images, which resembles the topographic image taken with a Pt–Ir tip (Fig. 1c). The DFT simulated SP-STM images (Fig. 2i) are composed of dumbbell-shaped protrusions centered at alternate Cr atoms and oriented along the two nearest top-layer Cl atoms, which well reproduce the experimental results. Note that both the SP-STM imaging and the DFT calculations indicate the antiferromagnetic coupling in the SW. Our calculation results do not support the existence of spiral magnetism in the classical magnetism picture and at the DFT level (Fig. S4). However, the inherent quantum (thermal) fluctuation in quasi-1D systems and the small MAE of 0.02 meV between the y and z directions (arising from vdW adsorption) could result in complex magnetic long-range ordering, which appears to be another elusive topic that requires further exploration.

The formation of the 1D phase differentiated the $NbSe_2$ substrate from the others. Thus, it was interesting to examine the competition between the 1D and 2D phases of $NbSe_2$. Figure 3a–d illustrates a sequence of topographic images of $CrCl_3/NbSe_2$ as a function of the total coverage (N_{total}) ranging from 0.035 ML to 0.36 ML, which showed that the 1D phase was dominant at a lower coverage (0.035 ML, Fig. 3a) and that the 2D phase became predominant for higher coverages (from 0.12 to 0.36 ML, Fig. 3b–d). This trend is more clearly depicted by a plot of the ratio (R_{1D}) between the partial coverage of the 1D wires N_{wire} and N_{total} as a function of N_{total} (black dotted line in Fig. 3e) in which R_{1D} continuously decrease. The plot of N_{wire} (red dashed line) also supports the dominance of the 2D phase at higher coverages because it first reaches a maximum at $N_{total} = 0.12$ ML and then decreases with further deposition of $CrCl_3$. The reduced N_{wire} is also accompanied by a narrowed average width of the 1D wires. Figure 3f plots the statistical width (w) distribution of the multi-wire arrays (MW) at two typical N_{total} values, namely, 0.12 and 0.36 ML.

Interestingly, an increase in N_{total} reduced the most-probable width of the MW from $w = 4$ to $w = 2$, implying a likely spontaneous transformation of the 1D phase into the 2D phase when the MW width exceeded a threshold (w_T).

Furthermore, such 1D–2D dimensionality conversion and the threshold width w_T were directly visualized in tip-controlled post-growth transformations. Figure 3g shows that a moderate tip stimulus precisely induced a transformation from a 1D wire array to a 2D nanoribbon (NR) at the nanometer scale ("Methods" section). Through substantive experimental attempts, we found that the wider the array was, the more readily the transformation occurred, and the transformation never occurred for $w < 4$. For instance, in the right-most region of Fig. 3g, the MW with $w = 3$ could retain its structure under all the considered tunneling conditions. Combining the as-grown and post-growth transformations, the w_T was estimated to be approximately three, which was well reproduced in our calculations, as shown in Fig. S8. This threshold width represents the crossover of the formation energies of the two phases; hence, it is crucial for comprehending the growth mechanism, as we will discuss in the following. Note that as the 2D phase was predicted to be in an XY FM state, the tip-induced structural transformations are, most likely, accompanied by changes of magnetism between 1D AFM and 2D FM states[14].

Our DFT results showed that the infinite 2D form of the $CrCl_3$ was 0.34 eV/Cr more stable than the infinite 1D form, which indicated that the edge-bulk energy competition of the 1D and 2D phases might play an essential role in stabilizing the 1D phase on the $NbSe_2$ substrate in the early growth stage. We thus focused on the relative stabilities of the SW and the 2D hexagonal flake (HF) containing the same finite number of Cr atoms, n_{Cr} (see Supplementary Fig. S9 for their atomic models). We found that the bulk unit indeed has lower energy than the edge (end) unit in both phases (Supplementary Table S2). Note that the ratio between the numbers of the end (edge) and bulk units in the SW is generally smaller than that in the HF, and the discrepancies in the ratio are n_{Cr}-dependent. For instance, with the smallest $n_{Cr} = 6$ (Fig. 4a, b), SW-6 contains two end units, while all six Cr atoms in HF-6 are edge units, yielding the largest difference in the edge(end)/bulk ratio. This might have accounted for the superior stability of the SW in the early growth stage.

However, the inferred superior stability of SWs could not be illustrated by directly comparing the total energies of HF-6 and SW-6 because of the unequal numbers of Cl atoms. The introduction of
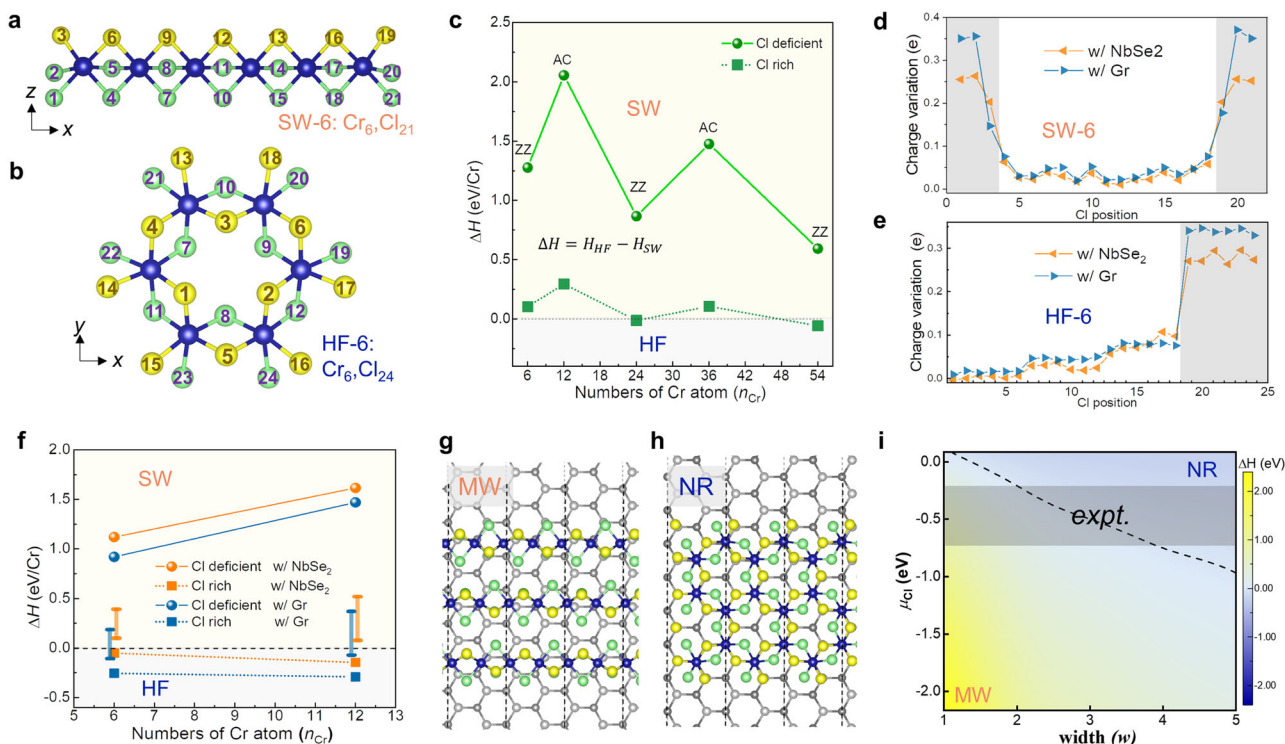
Fig. 4 | Theoretical understanding of the 1D phase growth and the 1D–2D transformation. a Side view of SW-6. **b** Top view of HF-6. The upper and lower surface Cl atoms are represented by yellow and green balls, respectively. **c** Plot of ΔH between the free-standing SW and HF at the Cl-rich (green square) and Cl-deficient (green circle) extremes as a function of n_{Cr}. The HFs with zig–zag (ZZ) edges (n_{Cr} = 6, 24, and 54) are more stable than the arm-chair (AC) ones (n_{Cr} = 12 and 36). **d, e** Plots of the charge variations for each individual Cl atom in SW-6 (**d**) and HF-6 (**e**) on the NbSe$_2$ (orange) and graphene (blue) substrates. The indices of

the Cl atoms are labeled in (**a, b**). The edge atoms are marked by gray shadows. **f** ΔH between SWs and HFs (at n_{Cr} = 6 and 12) with the substrates involved. The color-filled bars represent the estimated range of experimental μ_{Cl}. The circle and square symbols represent the results at the Cl-deficient and Cl-rich limits, respectively. **g, h** Atomic structures of the multi-wire array (MW, w = 3) on NbSe$_2$ and its corresponding nanoribbon (NR). **i** Phase diagram of ΔH as functions of w and μ_{Cl}. The contour line of ΔH = 0 is plotted as the dashed line. The shadow region corresponds to the experimental observation of w_T = 2–4.

the formation enthalpies, i.e., the consideration of the difference in the Cl number and the Cl chemical potential μ_{Cl}, solved this issue (see the "Methods" section for details of the formation enthalpy H and the total energies). Figure 4c plots the difference in the formation enthalpies of the HFs and their corresponding SWs for the Cl-rich (μ_{Cl} = 0.08 eV) and Cl-deficient (μ_{Cl} = −2.27 eV) limits ("Methods" section). The SW was found to be more stable (with a positive ΔH value) for both limits when n_{Cr} = 6. With increasing n_{Cr}, ΔH showed an overall declining tendency towards the negative regime. Although this declining trend implied a growth mode transformation from 1D wires to 2D flakes, these results could not explain the fact that the SW was solely formed on NbSe$_2$.

With the adsorption on both the NbSe$_2$ and BLG substrates, substantial charge transfer was identified in our calculation, especially at the ends (CrCl$_{4.5}$ units, Fig. 4d) or edges (CrCl$_4$ units, Fig. 4e). A total amount of 1.86 e was transferred from NbSe$_2$ to SW-6, primarily at the six end Cl atoms (-0.3 e/Cl, Fig. 4d), which stabilized the end unit with larger adsorption energy (Supplementary Tables S2 and S3). The delocalized π-orbital nature of the graphene electrons, along with the graphene work function and the energy levels of the SW (or HF) (Supplementary Fig. S10), led to an additional donated charge of 0.48 e for SW-6, further lowering its energy of the end unit (Supplementary Table S2). In comparison with the SWs, the HFs had a stronger ability to accept electrons, and 0.42 e and 0.50 e more electrons were transferred from the NbSe$_2$ and graphene substrates to HF-6, respectively, mainly around the outermost Cl edge atoms. These additionally transferred electrons provided extra stabilization for the 2D edges of the HF on the graphene substrate (Fig. 4e), on which E_{edge}^{HF} = −10.42 eV/ Cr was surprisingly lower than E_{bulk}^{SW} = −10.13 eV/Cr (Supplementary

Table S2). This partially or even fully broke the superior stability of the freestanding 1D phase in the early growth stage. Note that on the NbSe$_2$ substrate, the E_{edge}^{HF} = −10.13 eV/Cr remained higher than the E_{bulk}^{SW} = −10.23 eV/Cr, which favored the possibility of 1D phase growth. See Supplementary Table S2 for comprehensive results. The stronger charge transfer at the end (edge) results from their electron acceptor nature (valence of 3+ for Cr), while the structural relaxation plays a minor and passive role (Fig. S11).

This inferred favored growth was indeed reflected in the plot of ΔH between the HF and SW for n_{Cr} = 6 and 12 upon adsorption on the two substrates (Fig. 4f) for an experimentally estimated μ_{Cl}. In the following, we first discuss this estimation of μ_{Cl}. In practical experiments, the phase transformation mostly occurred from 1D MW to 2D NR rather than directly to hexagonal flakes. We compared the ΔHs between the MW and NR that formed on NbSe$_2$ with the equivalent width w (see Fig. 4g, h for their atomic models with w = 3 Cr rows). The phase diagram as functions of w and μ_{Cl} is displayed in Fig. 4i, where a black dotted line represents the contour line of ΔH = 0. According to the experimental fact that the most-probable width varied between w_T = 2 and 4 (Fig. 3f, g), we can estimate a range of experimental μ_{Cl} = −0.803 to −0.217 eV/Cl (shadow region in Fig. 4i).

In Fig. 4f, the color-filled bars represent the ranges of ΔH for the experimental range of μ_{Cl}. It is indeed shown that the 1D phase retained more stability throughout the whole experimental range of μ_{Cl} on the NbSe$_2$, while on graphene, the possibility of favoring the 2D growth appeared. These results demonstrated that the selective choice of a substrate with a proper ability to donate electrons could tune the 1D and 2D growth modes of CrCl$_3$ on the substrate. This new mechanism

is significantly distinct from the common notion of vdW epitaxy, in which the structure of the epilayer is nearly unrelated to the substrate[15].

Discussion

In conclusion, we demonstrated the first experimental realization of single-unit-cell-width $CrCl_3$ atomic wires and their stacked few-wire arrays on the surface of $NbSe_2$. The single $CrCl_3$ wire was identified as a new 1D polymorphic phase of the 2D magnetic material $CrCl_3$ with a large bandgap and an antiferromagnetic ground state. Rich emergent quantum phenomena are anticipated in this unprecedented hybrid system consisting of a vdW-integrated 1D spin chain/2D super-conductor. Moreover, a thorough understanding of the underlying growth mechanism revealed the elegant role of the electronic interactions at the vdW interface in controlling the dimensionality conversion and polymorphic phase transformation in epitaxial growth. This study expands the application scope of vdW interface engineering, offering an easy and flexible means to fabricate exotic 1D nanostructures.

Methods

Growth of $CrCl_3$

The $CrCl_3$ was grown on a freshly cleaved $NbSe_2$ substrate with a compound source molecular beam epitaxy (MBE). Anhydrous $CrCl_3$ powder of 99% purity was evaporated from a Knudsen cell. The growth speed of ~0.02 ML/min was determined by checking the coverages of the as-grown samples. The $NbSe_2$ substrate was kept at room temperature during growth. The BLG/SiC substrate was synthesized by silicon sublimation from the (0001) plane (Si face) of n-type 6H-SiC[29]. The optimal substrate temperature for the growth of the $CrCl_3$ monolayer flakes was ~500 K. Below this temperature, the $CrCl_3$ tended to form 2D fractal structure features on the bilayer graphene surface (for details, see Supplementary Fig. S12).

STM/S measurements

After sample preparation, the sample was inserted into a low-temperature scanning tunneling microscope (STM, Unisoku USM-1300) housed in the same ultra-high vacuum system. Polycrystalline Pt-Ir STM tip was used in our experiments. The bias voltage was applied to the sample. All STM images presented in this article were taken at 4.3 K. The dI/dV spectra were measured by using the lock-in technique with a reference signal at 963 Hz. The modulation amplitudes were set as 50 μV (Fig. 2e) and 10 mV for all other spectra. The SP-STM measurements were carried out via electrochemically etched Ni tips in a constant-current mode[30,31]. The spin-polarization of the Ni tip was calibrated on Co/Cu(111) (Supplementary Fig. S13), following the procedure reported in refs. 19,32,33, perpendicular magnetic fields of +0.7 T (−0.7 T) were used to magnetize the ferromagnetic Ni tip acquiring the spin-up (spin-down) tip state. The external fields were usually held for five minutes and then slowly reduced to zero. The magnetized tip was then used to perform STM imaging at 0 T in the same location.

Tip-induced phase transformation

The structural phase of the stacked wire arrays was not affected by imaging using a sample bias $0 V > V_B > -2.5 V$. Once the sample bias was in excess of ~−2.8 V, the transformation to the 2D phase could easily occur. The practical procedure we adopted for Fig. 3g was as follows: running continuous scanning of the selected region at the constant height mode with the initial scanning parameters of $V_B = -2.9 V, I = 3 pA$ until an abrupt drop of I (usually down to zero) was observed (since the 2D phase was slightly lower in terms of the topographic height).

DFT calculations

Calculations were performed using the generalized gradient approximation in the Perdew–Burke–Ernzerhof (PBE) form[34] for the

exchange-correlation potential, the projector augmented wave method[35], and a plane-wave basis set as implemented in the Vienna ab-initio simulation package (VASP)[36]. Dispersion corrections were made at the van der Waals density functional (vdW-DF) level[37] with the optB86b functional for the exchange potential (optB86b-vdW)[38] in all structural relaxations. The structures were fully relaxed until the residual force per atom was less than 0.005 (0.02) eV/Å for free-standing (substrate-supported) SWs and HFs. On-site Coulomb interactions on the Cr d orbitals were considered using a DFT + U method[39] with $U = 3.9$ eV and $J = 1.1$ eV, consistent with the values used in the literature[40]. A vacuum layer larger than 15 Å was used in all supercells to avoid interactions between the slabs of adjacent supercells. An energy cut-off of 700 (400) eV was used for the plane wave basis set in calculating free-standing (substrate-supported) structures. A k-mesh of $14 \times 1 \times 1$ was used to sample the first Brillouin zone of freestanding infinite SWs, while the Gamma point was used in other calculations.

The PBE functional was used in the comparison of relative energies of individual configurations based on the atomic structures optimized using the optB86b-vdW functional. Spin–orbit coupling was considered in all energy comparisons. The accuracy of such a set of methods was well tested in calculations on many 2D magnets[41–48] The charge transfer between the SWs (HFs) and the substrate was evaluated using the Bader charge analysis method[49]. The charge variation of a Cl atom was defined as the Bader charge of the Cl atom in SW-6 (HF-6) being placed on the substrate minus that in the free-standing form. The phonon dispersion was calculated using the density functional perturbation theory, as implemented in the PHONOPY code[50].

The periodic direction of the multi-wires array (zig–zag direction of the corresponding nanoribbon) is oriented along the arm-chair direction of $NbSe_2$, which was consistent with the experimental observation. For the finite SWs and HFs with a $NbSe_2$ or graphene substrate, we used the same relative orientations as the periodic case. Two-layer $NbSe_2$ (graphene) was used to model the substrate, in which the bottom layer was kept fixed, and the top layer was allowed to fully relax.

Calculation of formation enthalpy H

The formation enthalpy H for finite SW and HF is defined as $H = (E_{total}^{HF/SW} - n_{Cr} \bullet \mu_{Cr} - n_{Cl} \bullet \mu_{Cl})/n_{Cr}$. $E_{total}^{HF/SW}$ is the total energy of SW or HF, $n_{Cr}(n_{Cl})$ is the number of Cr (Cl) atoms. The chemical potentials of Cr and Cl in $CrCl_3$ fulfill the equation $\mu_{Cr} + 3\mu_{Cl} = \mu_{Cr}^* + 3\mu_{Cl}^* + \triangle H_{CrCl_3}$, where μ_{Cr}^* is the chemical potential of Cr in the bulk form, μ_{Cl}^* is the chemical potential of Cl_2 and $\triangle H_{CrCl_3}$ is the formation energy of $CrCl_3$. At the Cl rich limit, one gets $\mu_{Cl} = \mu_{Cl}^*$, while at Cl deficient limit, $\mu_{Cl} = \mu_{Cl}^* + \triangle H_{CrCl_3}/3$.

The total energy reads $E_{total}^{HF/SW} = n_{edge}^{HF/SW} \times (E_{edge-fs}^{HF/SW} + E_{edge-ad}^{HF/SW}) + n_{bulk}^{HF/SW} \times (E_{bulk-fs}^{HF/SW} + E_{bulk-ad}^{HF/SW}) + E_{SEC}^{HF/SW}$. If we set $E_{edge}^{HF/SW} = E_{edge-fs}^{HF/SW} + E_{edge-ad}^{HF/SW}$ and $E_{bulk}^{HF/SW} = E_{bulk-fs}^{HF/SW} + E_{bulk-ad}^{HF/SW}$, it further reads $E_{total}^{HF/SW} = n_{edge}^{HF/SW} \times E_{edge}^{HF/SW} + n_{bulk}^{HF/SW} \times E_{bulk}^{HF/SW} + E_{SEC}^{HF/SW}$, where subscripts "edge" and "bulk" refer to edge and bulk units of SW and HF, postfixes "-fs" and "-ad" denote free-standing and adsorbed forms of the $CrCl_x$ units, n is the number of $CrCl_x$ units in a finite size SW or HF, subscript "SEC" stands for spin-exchange coupling.

In order to determine the relative stability of the SW and HF phases with the same n_{Cr}, we could examine the difference of normalized enthalpy $\Delta H_{HF-SW} = [(n_{edge}^{HF} \times E_{edge}^{HF} + n_{bulk}^{HF} \times E_{bulk}^{HF}) - (n_{edge}^{SW} \times E_{edge}^{SW} + n_{bulk}^{SW} \times E_{bulk}^{SW}) + (E_{SEC}^{HF} - E_{SEC}^{SW}) + \triangle n_{Cl} \bullet \mu_{Cl}]/n_{Cr}$, where Δn_{Cl} indicates the number difference of Cl atoms between the SW and HF phases. A ΔH_{HF-SW} value larger (smaller) than zero indicates the superior stability of SW (HF). Here, the magnetic term is considerably smaller than other terms and is thus negligible in comparing relative energy of SW and HF. Number n_{edge}^{SW} always equals to 2 in a finite SW and number n_{bulk}^{HF} is often smaller than n_{edge}^{HF} or even approaches zero in

a small-size HF. We could consider a simplified and qualitative relation $\Delta H_{HF-SW} \sim E_{edge}^{HF} - E_{bulk}^{SW} + (\Delta n_{Cl} \bullet \mu_{Cl})/n_{Cr}$ to judge the relative stability of SW and HF by assuming $E_{edge}^{HF} \approx E_{bulk}^{HF}$ and $E_{bulk}^{SW} \approx E_{edge}^{SW}$. Thus, if E_{bulk}^{SW} is lower than E_{edge}^{HF}, we could have chance to obtain a positive $\triangle H_{HF-SW}$ and thus more stable SW in a certain μ_{Cl} range as derived from the experiments.

Data availability

The data that support the findings of this study are available within the article and its Supplementary Information. The source data are available from the corresponding authors upon request.

Code availability

The code that supports the findings of this study is available from the corresponding author upon reasonable request.

References

1. Karakachian, H. et al. One-dimensional confinement and width-dependent bandgap formation in epitaxial graphene nanoribbons. *Nat. Commun.* **11**, 6380 (2020).
2. Chen, Y.-C. et al. Tuning the band gap of graphene nanoribbons synthesized from molecular precursors. *ACS Nano* **7**, 6123–6128 (2013).
3. Yan, L. & Liljeroth, P. Engineered electronic states in atomically precise artificial lattices and graphene nanoribbons. *Adv. Phys.* **4**, 1651672 (2019).
4. Yu, Y. et al. Phase-controlled growth of one-dimensional Mo_6Te_6 nanowires and two-dimensional $MoTe_2$ ultrathin films heterostructures. *Nano Lett.* **18**, 675–681 (2018).
5. Xia, Y. et al. Quantum confined Tomonaga–Luttinger liquid in Mo_6Se_6 nanowires converted from an epitaxial $MoSe_2$ monolayer. *Nano Lett.* **20**, 2094–2099 (2020).
6. Deng, J. et al. Precise tuning of band structures and electron correlations by van der Waals stacking of one-dimensional W_6Te_6 wires. *Nano Lett.* **20**, 8866–8873 (2020).
7. Huang, B. et al. Layer-dependent ferromagnetism in a van der Waals crystal down to the monolayer limit. *Nature* **546**, 270–273 (2017).
8. Gong, C. et al. Discovery of intrinsic ferromagnetism in two-dimensional van der Waals crystals. *Nature* **546**, 265–269 (2017).
9. Deng, Y. et al. Gate-tunable room-temperature ferromagnetism in two-dimensional Fe_3GeTe_2. *Nature* **563**, 94–99 (2018).
10. Fei, Z. et al. Two-dimensional itinerant ferromagnetism in atomically thin Fe_3GeTe_2. *Nat. Mater.* **17**, 778–782 (2018).
11. O'Hara, D. J. et al. Room temperature intrinsic ferromagnetism in epitaxial manganese selenide films in the monolayer limit. *Nano Lett.* **18**, 3125–3131 (2018).
12. Chen, W. et al. Direct observation of van der Waals stacking–dependent interlayer magnetism. *Science* **366**, 983–987 (2019).
13. Kezilebieke, S. et al. Topological superconductivity in a van der Waals heterostructure. *Nature* **588**, 424–428 (2020).
14. Bedoya-Pinto, A. et al. Intrinsic 2D-XY ferromagnetism in a van der Waals monolayer. *Science* **374**, 616–620 (2021).
15. Liu, Y., Huang, Y. & Duan, X. Van der Waals integration before and beyond two-dimensional materials. *Nature* **567**, 323–333 (2019).
16. Fu, L., Shang, C., Zhou, S., Guo, Y. & Zhao, J. Transition metal halide nanowires: a family of one-dimensional multifunctional building blocks. *App. Phys. Lett.* **120**, 023103 (2022).
17. Choi, D.-J. et al. Colloquium: atomic spin chains on surfaces. *Rev. Mod. Phys.* **91**, 041001 (2019).
18. Nadj-Perge, S. et al. Observation of Majorana fermions in ferromagnetic atomic chains on a superconductor. *Science* **346**, 602–607 (2014).
19. Jeon, S. et al. Distinguishing a Majorana zero mode using spin-resolved measurements. *Science* **358**, 772–776 (2017).
20. Jack, B., Xie, Y. L. & Yazdani, A. Detecting and distinguishing Majorana zero modes with the scanning tunnelling microscope. *Nat. Rev. Phys.* **3**, 541–554 (2021).
21. Kim, H. et al. Toward tailoring Majorana bound states in artificially constructed magnetic atom chains on elemental superconductors. *Sci. Adv.* **4**, eaar5251 (2018).
22. Renard, J.-P., Regnault, L.-P. & Verdaguer, M. *Magnetism: Molecules to Materials I: Models and Experiments*. (Wiley-VCH, Weinheim, Germany, 2002).
23. Sahling, S. et al. Experimental realization of long-distance entanglement between spins in antiferromagnetic quantum spin chains. *Nat. Phys.* **11**, 255–260 (2015).
24. Simon, J. et al. Quantum simulation of antiferromagnetic spin chains in an optical lattice. *Nature* **472**, 307–312 (2011).
25. Zhang, W. et al. Flat epitaxial quasi-1D phosphorene chains. *Nat. Commun.* **12**, 5160 (2021).
26. Li, S. et al. Robust half-metallicity in transition metal tribromide nanowires. *Nanoscale* **10**, 15545–15552 (2018).
27. Wiesendanger, R. Spin mapping at the nanoscale and atomic scale. *Rev. Mod. Phys.* **81**, 1495–1550 (2009).
28. Bode, M. et al. Chiral magnetic order at surfaces driven by inversion asymmetry. *Nature* **447**, 190–193 (2007).
29. Wang, Q. et al. Large-scale uniform bilayer graphene prepared by vacuum graphitization of 6H-SiC(0001) substrates. *J. Phys. Condens. Matter* **25**, 095002 (2013).
30. Cavallini, M. & Biscarini, F. Electrochemically etched nickel tips for spin polarized scanning tunneling microscopy. *Rev. Sci. Instrum.* **71**, 4457–4460 (2000).
31. Chen, H., Xiao, W., Wu, X., Yang, K. & Gao, H.-J. Electrochemically etched Ni tips in a constant-current mode for spin-polarized scanning tunneling microscopy. *J. Vac. Sci. Technol. B* **32**, 061801 (2014).
32. Xing, Y. et al. Localized spin-orbit polaron in magnetic Weyl semimetal $Co_3Sn_2S_2$. *Nat. Commun.* **11**, 5613 (2020).
33. Zhang, H. H. et al. Majorana zero mode detected with spin selective Andreev reflection in the vortex of a topological superconductor. *Phys. Rev. Lett.* **116**, 257003 (2016).
34. Perdew, J. P., Burke, K. & Ernzerhof, M. Generalized gradient approximation made simple. *Phys. Rev. Lett.* **77**, 3865–3868 (1996).
35. Blöchl, P. E. Projector augmented-wave method. *Phys. Rev. B* **50**, 17953–17979 (1994).
36. Kresse, G. & Furthmüller, J. Efficient iterative schemes for ab initio total-energy calculations using a plane-wave basis set. *Phys. Rev. B* **54**, 11169–11186 (1996).
37. Dion, M. et al. Van der Waals density functional for general geometries. *Phys. Rev. Lett.* **92**, 246401 (2004).
38. Klimeš, J. et al. Van der Waals density functionals applied to solids. *Phys. Rev. B* **83**, 195131 (2011).
39. Anisimov, V. I. et al. First-principles calculations of the electronic structure and spectra of strongly correlated systems: the LDA+U method. *J. Phys. Condens. Matter* **9**, 767–808 (1997).
40. Li, P. et al. Single-layer CrI_3 grown by molecular beam epitaxy. *Sci. Bull.* **65**, 1064–1071 (2020).
41. Wang, C. et al. Layer and doping tunable ferromagnetic order in two-dimensional CrS_2 layers. *Phys. Rev. B* **97**, 245409 (2018).
42. Wang, C. et al. A family of high-temperature ferromagnetic monolayers with locked spin-dichroism-mobility anisotropy: MnNX and CrCX (X = Cl, Br, I; C = S, Se, Te). *Sci. Bull.* **64**, 293 (2019).
43. Jiang, P. et al. Stacking tunable interlayer magnetism in bilayer CrI_3. *Phys. Rev. B* **99**, 144401 (2019).
44. Wang, C. et al. Bethe-Slater-curve-like behavior and interlayer spin-exchange coupling mechanisms in two-dimensional magnetic bilayers. *Phys. Rev. B* **102**, 020402 (2020).
45. Cheng, X. et al. Light helicity detector based on 2D magnetic semiconductor CrI_3. *Nat. Commun.* **12**, 6874 (2021).

46. Li, B. et al. Van der Waals epitaxial growth of air-stable $CrSe_2$ nanosheets with thickness-tunable magnetic order. *Nat. Mater.* **20**, 818–825 (2021).

47. Xian, J. et al. Spin mapping of intralayer antiferromagnetism and field-induced spin reorientation in monolayer $CrTe_2$. *Nat. Commun.* **13**, 257 (2022).

48. Gu, P. et al. Magnetic phase transitions and magnetoelastic coupling in a two-dimensional stripy antiferromagnet. *Nano Lett.* **22**, 1233 (2022).

49. Henkelman, G. et al. A fast and robust algorithm for Bader decomposition of charge density. *Comput. Mater. Sci.* **36**, 354–360 (2006).

50. Togo, A. & Tanaka, I. First principles phonon calculations in materials science. *Scr. Mater.* **108**, 1–5 (2015).

Author contributions

S.Z.L., Z.B.C., and Y.P.G. carried out the MBE growth and STM/S measurements. D.P.G. and J.W. performed the first-principles calculations. J.H.D. and Y.S.B. contributed to the sample preparation and STM measurements. Z.B.C. completed the SP-STM characterization. C.T. and Y.G.S coordinated the preparations of NbSe2. C.W. and L.W.Z participated in discussions of theoretical calculations. J.H. and C.D.Z. initiated and coordinated the work, participated in the experiments, analyzed data. W.J. conceived the theoretical calculations and analysis. S.Z.L., D.P.G., J.H., J.W., and C.D.Z. wrote the paper with inputs from the other co-authors.

Competing interests

The authors declare no competing interests.

Additional information

Supplementary information The online version contains supplementary material available at https://doi.org/10.1038/s41467-023-38175-4.

Correspondence and requests for materials should be addressed to Jun He, Wei Ji or Chendong Zhang.

Peer review information *Nature Communications* thanks David Serrat, Vei Wang, and the other anonymous reviewer(s) for their contribution to the peer review of this work.

Reprints and permissions information is available at http://www.nature.com/reprints

Publisher's note Springer Nature remains neutral with regard to jurisdictional claims in published maps and institutional affiliations.